NUMERICAL INVESTIGATION OF THE IMPELLER BLADES, MANUFACTURED BY METAL 3D PRINTING TECHNOLOGY WITH INTERNAL STRUCTURES

JAKUB STARECEK[1], VACLAV PREJDA[1], PROKOP MORAVEC[1], PETR ABRAHAMEK[2], LUKAS ZAVADIL[2], TOMAS KRATKY[1], HANA DOLAKOVA[3], MIROSLAV MASLAN[3]

[1]CENTRE OF HYDRAULIC RESEARCH,

[2]SIGMA Research & Development Institute,

Lutin, Czech Republic

[3]Palacky University Olomouc,

Czech Republic

DOI: 10.17973/MMSJ.2022_06_2022082

j.starecek@sigma.cz

This paper presents the results of FEM (Finite Element Method), CFD (Computational Fluid Dynamics) and modal analyses of model semi-axial pump. Two sets of impeller blades were printed by metal 3D printing technology with internal honeycomb structures. The set of solid blades, manufactured by CNC machining for a comparison, was also included. 3D printed blades were designed with internal structures in order to save material, and with respect to mechanical and dynamic properties. Saved material can change the starting moment, modulate modal properties or decrease strength properties. The 3D printed blades can be produced very quickly and with accurate blade surface finish. One of the reasons of this approach can be the use of 3D printed blades as spare parts for industrial applications or for model pump research. This paper contains short introduction to blade design with internal honeycomb structures and their one-way FSI analyses (Fluid Structure Interaction). The final results of best design are presented and discussed.

KEYWORDS

Pump, Impeller, 3D Printing, CFD, FEM, Modal Analysis, Honeycomb, Internal, Structures

1 INTRODUCTION

The hydrodynamic semi-axial pump with blade diffuser was designed at the Centre of Hydraulic Research. The model consists of right-angle draft tube, pump impeller with eight impeller blades, welded blade diffuser with seven blades, and right-angle elbow on the outlet. This pump was characterized by specific speed $n_s = 360\ \mathrm{min}^{-1}$. Specific speed was calculated by following equation (1) [Paciga 1984]:

$$n_s = 3{,}65 \cdot n \cdot \frac{Q^{0{,}5}}{H^{0{,}75}} \tag{1}$$

where n is rotor speed per minute (RPM) [min^{-1}], Q represents mass flow [$\mathrm{m}^3 \cdot \mathrm{s}^{-1}$] and H [m] is pump total head. The design point was set to H = 25 m; Q = 330 $\mathrm{l} \cdot \mathrm{s}^{-1}$ and RPM = 1920 min^{-1}. The model pump impeller is not fully regulated. Regulation mechanisms does not fit in the hub, so the pitching must be ensured manually. Bigger industrial pumps, which are obtained by affine (model) conversion, can change pitch angle of the impeller blades on demand during the operation. In both cases, blades are supported by pivots in the hub. In case of model pump, pivots are supported by nuts. The pump operating range can be changed by various pitch angle. Whole pump design has been completed by analytical calculation, and shape optimization was performed by numerical simulations. Shape optimization was focused on maximal efficiency and position of BEP (Best Efficiency Point). Total head was taken into account [Karassik 2012]. For simulations which are the subject of this article, only data which corresponded with BEP for zero pitch angle position were used. Visualization of the final design of pump impeller is shown in Figure 1.

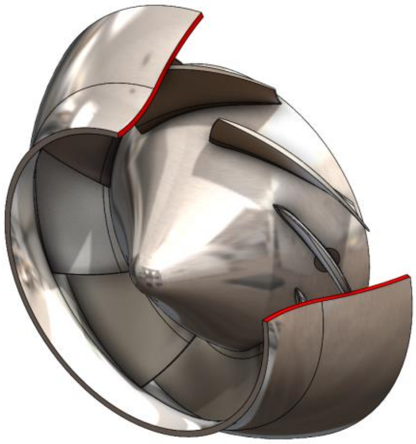

Figure 1. 3D model of pump impeller. Blades were manufactured by 3D printing technology

In the next step, the internal honeycombs structures were designed and optimized. There were two main intentions when considering the honeycombs structure. First, such structure allows for lowering the weight of the impeller and consequently the starting moment. Second, changing the blade internal structure and its mass distribution can also alter the dynamic behaviour of the blade, and its deformations induced by the fluid dynamics. The blade body consisted of honeycomb structure with solid material situated around pivots, due to the formation of a thread. Solid material was also around blade radius for increasing strength and decreasing stress. Blade final mechanical properties, with focus on blade-pivot connection, were analysed in terms of strength and stress by FEM analyses. As a result, this article deals with the pump design and flow analyses by CFD simulation. The second part is focused on honeycomb structures design, their structural and modal analyses, types of honeycombs and their properties. FEM simulations were performed as one-way FSI analyses. All results in this article were evaluated by numerical simulations, using ANSYS tools. The same approach was carried out for optimisation of blades in gas turbine and their inner structures. The thermal and strength properties were included into account [Pal 2020]. Overview of 3D printing technologies and possibilities for turbomachinery for our inspiration is from [Novotny 2019], [Abhinav 2020] and [Wang 2019].

2 NUMERICAL SIMULATION

The impeller and diffuser blades were modelled separately by using ASNYS BladeGen. The outlet diameter of the impeller was set as $D_{2,o}$ = 348 mm in outer streamline and $D_{2,I}$ = 249 mm in inner streamline. Whole basic design analytic process is described in [Gulich 2014]. ANSYS Turbogrid, ICEM CFD and ANSYS Meshing were used for computational mesh generation.

The blade domains were meshed with hexahedral cells. Inlet pipe with draft tube, diffuser and outlet elbow were meshed with tetrahedral cells. All parts were meshed with respect to boundary layer refinement. Automatic wall function was chosen for boundary layer computation. Complete CFD model consisted of approximately 2 500 000 nodes and 3 160 000 cells. The CFD simulations were performed as fully transient with ANSYS CFX, where timestep was equal to 2,5° of impeller rotation, with three internal iterations. The Shear Stress Transport (SST) turbulence model was used for all simulations. Figure 2 represents boundary conditions, which were used for simulations. All partially transparent parts were set as stationary no-slip walls, so the surface roughness was not included in simulations. The General Grid Interface (GGI) was applied between stationary domains and rotating impeller domain – marked by yellow color in Figure 2. Zero total pressure was set at the inlet – marked by blue color in Figure 2. Current mass flow rate was set at the outlet – marked by red color in Figure 2. The reference pressure P_{ref} = 1 atm was set for whole simulation in each partial domain. Water with temperature T = 25 °C was set as transported medium. The impeller blade gap was included in the CFD model, and was set up as t = 0,3 mm. Mechanical losses inside bearings and mechanical friction losses were not included in simulations. The cavitation effect was neglected. The fluid flow was considered as incompressible and isothermal.

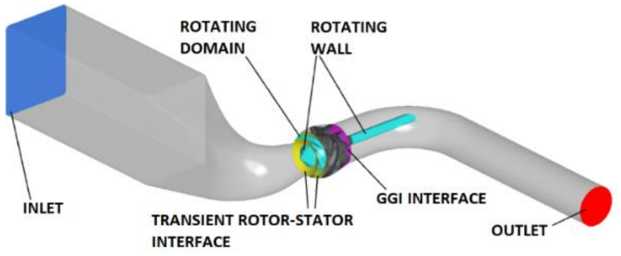

Figure 2. Visualization of the CFD model with boundary conditions

2.1 *Pump head and hydraulic efficiency definition*

Three main performance quantities were evaluated during design process by numerical simulations. First parameter was pump head H_{pump} [m], which is defined by pressure difference:

$$H_{pump} = \frac{\Delta p_{pump}}{g \cdot \rho} = \frac{p_{tot,OUTLET} - p_{tot,INLET}}{g \cdot \rho} \qquad (2)$$

where Δp_{pump} [Pa] represents total pressure difference between inlet and outlet face in computational domain in Figure 2. Constant ρ [$kg \cdot m^{-3}$] represents water density and g [$m \cdot s^{-2}$] gravitational acceleration. Second parameter was hydraulic efficiency:

$$\eta_h = \frac{P_{in}}{P} = \frac{(p_{tot,OUTLET} - p_{tot,INLET}) \cdot Q}{2 \cdot \pi \cdot n \cdot M_k} \cdot 100 \qquad (3)$$

where P_{in} [W] represents hydraulic output and P [W] represents hydraulic input. Torque M_k [N·m] was calculated from all rotational parts (rotational faces). Variable n [min^{-1}] is rotational speed and Q [$m^3 \cdot s^{-1}$] represent mass flow. The IEC 60 193 standard [IEC 60 193] was used for hydraulic parameters definition.

2.2 *Results of CFD analyses*

The main results from CFD simulations were hydraulic output parameters (performance characteristics), defined in previous chapter. In following Figures 3 and 4, pump output parameters are presented - on the horizontal axis is defined mass flow, as ratio between current mass flow and mass flow in design point. Total head H was defined by equation (2) and hydraulic efficiency η_h was defined by equation (3).

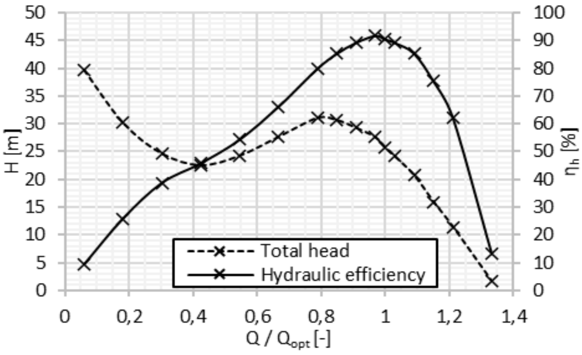

Figure 3. Hydraulic output parameters of model pump

The BEP corresponds with design point, total head is also in accordance with the specification. The Q – H curve instability is manifested less than Q/Q_{opt} = 0,8 of design point. Figure 4 represents hydraulic input, which depends on torque and RPM. The definition of hydraulic input represents denominator in equation (3) and was determined as P = 90 kW for design point.

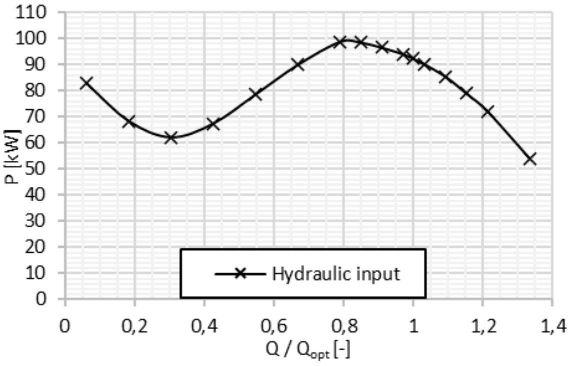

Figure 4. Hydraulic input parameters of model pump

The FEM analyses of the static pressure action on impeller blades were provided in the following step. Sets of solid blades and also honeycomb structures were tested. The next chapter discusses this issue.

3 FEM ANALYSIS

In the next step, static pressure fields from CFD simulations (located on the impeller blade surface and hub surface) were imported to transient FEM analyses, as *.csv data files. For the structural analyses and modal analyses was used reduced model, which contained only impeller hub, hub lid, eight impeller blades and KM nut with washers. The reduced model is visualized in Figure 5.

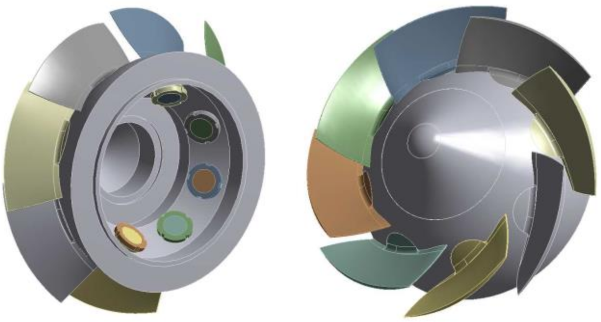

Figure 5. Reduced model for the transient structural analyses

All variants of the internal honeycomb structures and solid blade were evaluated and compared by mechanical properties. The results were evaluated according to the valid standards [NTD A.S.I.]. After exploring various types of design (honeycomb structures, lattice structures, waves structures, pyramid structures) and their shape or size optimization, three types of internal structures were chosen due to their strength properties and acceptable simulation complexity. In Figure 6, the differences between internal structures are visualised. Thickness of the blade envelope (blade surface) is t_1 = 1 mm and thickness of the honeycomb structure wall is t_2 = 2mm for both cases (honeycomb wall thickness). Variable s [mm] represent hexagon side length:

a) Solid blade without internal honeycomb structures.
b) Coarse hexahedral honeycomb structures - s = 9 mm
c) Fine hexahedral honeycomb structures - s = 4,5 mm

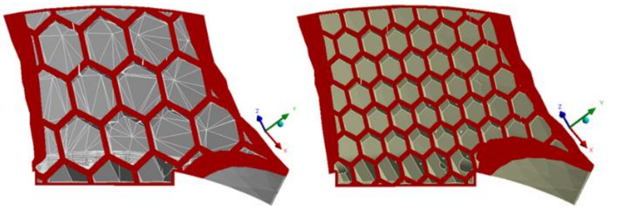

Figure 6. Difference between coarse and fine honeycomb structures. Left – coarse hexahedral structures (b); Right – fine hexahedral structures (c)

Computational mesh consists of 1 557 048 tetrahedral elements and 2 322 707 nodes in the case with solid impeller blades. Blades with internal structures have approximately the same number of cells. The mesh refinements were used in the blade root part (Figure 7).

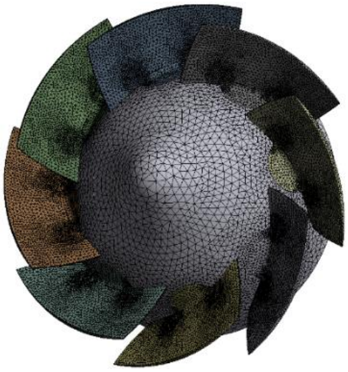

Figure 7. Computational tetrahedral mesh for transient structural analyses

3.1 *Material properties and FEM analyses setup*

All impeller parts were made from stainless steel 1.4301. This stainless steel was used also for 3D printing technology as printing material. Isotropic material was the main premise of this task. Material properties which were included to the numerical analyses for both printed cases and solid blade were summarized in Table 1 [MAT.1.4301]. Special ANSYS modules for simulating 3D printed parts were not included into solution.

Constant name	Constant	Unit	Value
Young's Modulus	E	[MPa]	199 000
Coefficient of thermal expansion	α	[K^{-1}]	$16{,}0 \cdot 10^{-6}$
Density	ρ	[$kg \cdot m^{-3}$]	7 850
Yield strength	$R^T{}_{p0,2}$	[MPa]	186
Ultimate strength	$R^T{}_m$	[MPa]	490
Elongation	A_5	[%]	40
Contraction	Z	[%]	50
Poisson ratio	μ	[-]	0,3

Table 1. Material properties of stainless-steel 1.4301 for solid blade.

FEM analyses were set as fully transient. The analyses ended with two complete impeller revolutions. Timestep was set as t = 0,00021704 s, which is equal to 2,5° of impeller rotation per one timestep, as in the CFD simulation. The whole simulation had 288 timesteps and in each timestep the static pressure field was imported to FEM analysis and structural simulation was calculated. Only last 144 timesteps were chosen as relevant data for following evaluation. The main reason why the last 144 timesteps are evaluated is the stability and reduction of residuals peaks from the first revolution. The impeller rotation was set as Remote Displacement boundary condition. Imported static pressure was also set as boundary condition. In Figure 8, there is visualized imported static pressure field on the impeller blades and hub.

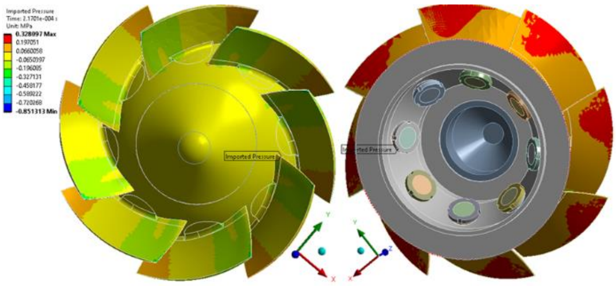

Figure 8. Static pressure field imported to the FEM analysis (last timestep)

3.2 *Results of FEM analyses*

The FEM analyses of the blade were evaluated for the timestep with the maximal stress intensity within the revolution for pump regime: Q/Q_{opt} = 1 (Design Point). The maximal stress depends on the position on the impeller and stator in the pump. Each type of the blade internal structure designs was evaluated and analysed in the most critical areas and for the most critical timestep. It is possible to predict the most critical areas on the suction and pressure side, especially close to blade root, across the stick radius of the blade. Maximal stress for the solid blade design was evaluated in two blade sections (marked as: A-A and C-C). Section A-A was located close to leading edge area (LE). Section C-C was located close to trailing edge area (TE) of the solid blade. All sections on the blades were defined through the wall. The evaluated paths for the honeycomb structure blades are only through the wall of the blade surface. For the solid blade there were visualized directions of sections in Figure 9.

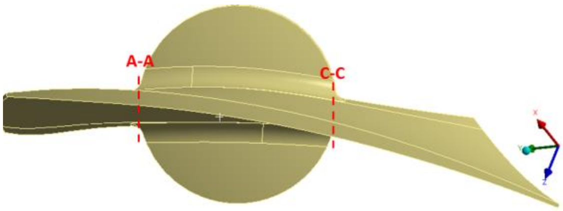

Figure 9. Section definition for the solid blade

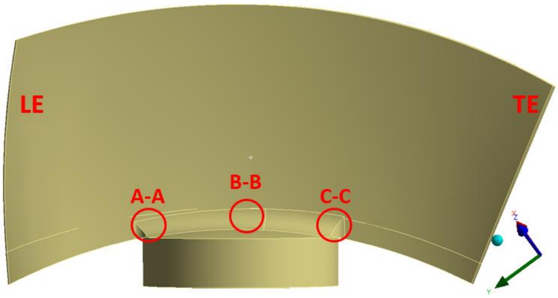

Figure 10. Section areas for the honeycomb structures blades

For the blades with internal honeycomb structures, it was also necessary to evaluate the third section in the middle of the blade, as shown in Figure 10. The length of each section through the blade is defined by variable l [mm]. This variable was used in the following decomposition of the stress, it is visualized in Figure 11. The stress on the blades was evaluated by stress intensity definition in ANSYS Workbench [ANSYS 2022]. The definition of the stress intensity σ_I [MPa] is described in following equation (4), where $\sigma_1 - \sigma_2$, $\sigma_2 - \sigma_3$ and $\sigma_3 - \sigma_1$ represents the difference between maximal values of main stress.

$$\sigma_I = MAX(|\sigma_1 - \sigma_2|, |\sigma_2 - \sigma_3|, |\sigma_3 - \sigma_1|) \qquad (4)$$

For the maximal stress intensity evaluation on the blades, we need to decompose stress intensity into basic components. This decomposition was created by linearized stress intensity in ANSYS Workbench. Basic components of stress are compared with permissible values and are defined as follows:

-	membrane stress	σ_m	[MPa]
-	bending stress	σ_b	[MPa]
-	membrane + bending stress	σ_{m+b}	[MPa]
-	peak stress	σ_p	[MPa]
-	total stress	σ_{total}	[MPa]

Obtained results were evaluated according to [NTD A.S.I. Section 3]. For static analyses it was used sum of membrane and bending stress (σ_{m+b}). For example, Figure 11 represents one of the linearized decompositions used during evaluation of solid blade in A-A section. In this chart three main basic components σ_m, σ_{m+b} and σ_{total} were visualized as the function of section length, where value l = 8,6 mm represent section length for solid blade. The values of σ_{m+b} and σ_{total} are variables along the length of the section, but σ_m is constant for the whole section.

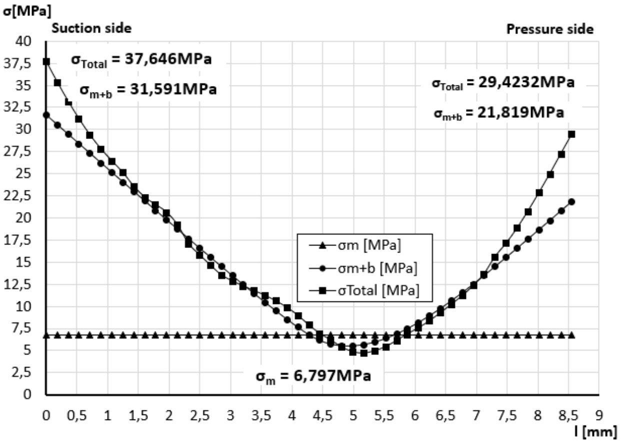

Figure 11. Linearized stress intensity decomposition for solid blade at A-A section

Solid blade

The position of the section for linearized decomposition are marked by red circles include the maximal stress of stress intensity. The highest value of the stress is the reason for choosing σ_{m+b}. The shape differences and locally increased stress values for solid blade are visualized in Figure 12. The maximum value for evaluation on this blade is σ_{m+b} = 31,59 MPa.

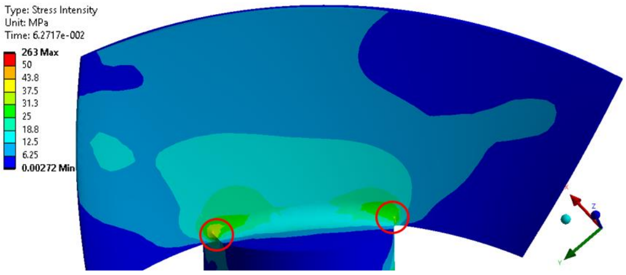

Figure 12. Stress intensity on the pressure side of the solid blade

In Figure 13, there was visualized stress intensity distribution on the perpendicular blade section. Increasing stress intensity outwards the blade could be detected in the picture. Maximal stress intensity was located on the blade surface and on the blade radius.

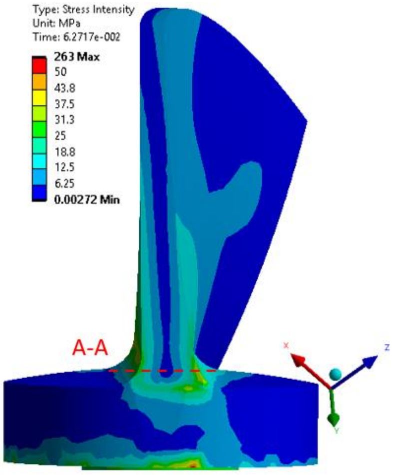

Figure 13. Section A-A for linearized decomposition of stress on solid blade

Blades with internal structures

The second design was the blade with internal coarse honeycomb structure. It is possible to observe the highest stress values close to A-A and B-B sections, as shown in Figure 14. These internal structures were characterized by different internal shapes with internal edges. It works as a stress concentrator and maximal stress were evaluated inside the blade on internal structures edges situated close the blade radius.

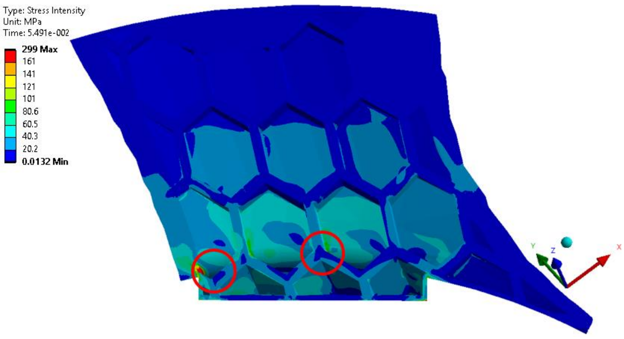

Figure 14. Stress intensity distribution inside the blade with coarse honeycomb structure

In Figure 15, there were visualized perpendicular sections A-A and B-B of the coarse honeycomb blade. It is possible to detect maximal stress intensity situated on the blade radius and around internal structures.

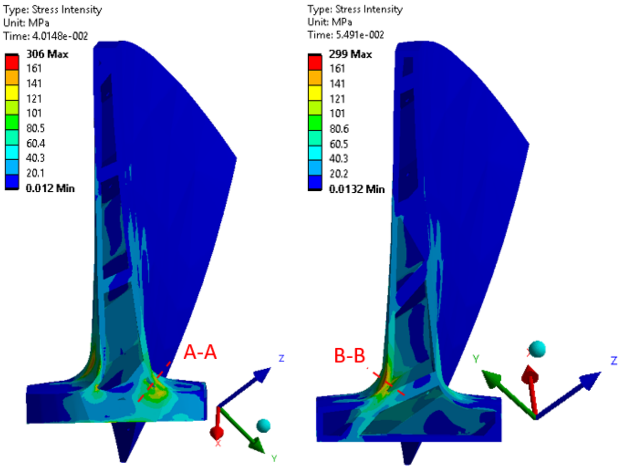

Figure 15. Sections A-A and B-B for linearized decomposition of stress on blade with coarse honeycomb structures

Fine honeycomb structure was third design. This blade design had also critical points in the section B-B and C-C. In Figure 16, there were visualized critical areas, which were situated usually close to the internal structures.

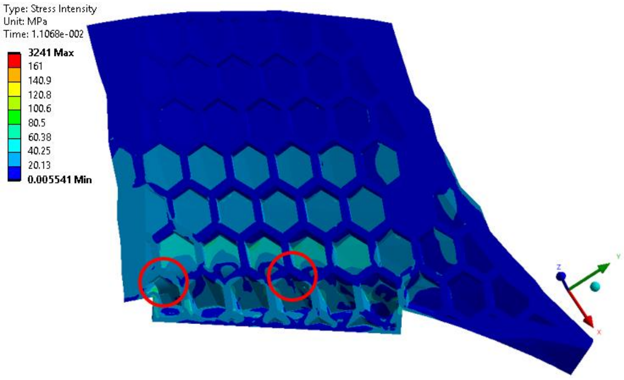

Figure 16. Stress intensity distribution inside blade with fine honeycomb structure

In Figure 17, there were visualized two critical perpendicular sections B-B and C-C on the blade with fine honeycomb structure. It is possible to deduce that fine internal structure can evenly distribute maximal stress and decrease local stress peaks.

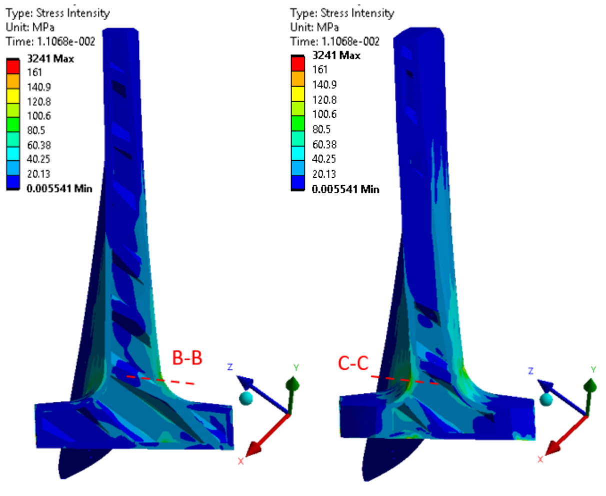

Figure 17. Section B-B and C-C for linearized decomposition of stress on blade with fine internal structures

Safety factor was the main factor to determine the quality of internal structure design. Safety factor is defined by variable K [-]:

$$K = \frac{\sigma_D}{\sigma_E} \tag{5}$$

where $\sigma_E = \sigma_{m+b}$ is stress which was evaluate from FEM analysis for this case and σ_D is permissible value of stress. Permissible value σ_D [MPa] is determined according to the standards [NTD A.S.I. Section 3]. Specifically in this case, the value was determined according to the equation (6).

$$\sigma_D = 1{,}3 \cdot \sigma \tag{6}$$

The variable σ [MPa] is defined as nominal permissible value of stress. The procedure for determining this value of stress is visualized in equation (7).

$$\sigma = min\left\{\frac{R^T_{p0,2}}{1{,}5}; \frac{R^T_m}{2{,}6}\right\} \tag{7}$$

Constants $R^T_{p0,2}$ [MPa] represent yield strength of material and R^T_m [MPa] is ultimate strength of material for constant temperature, used constant values are shown at Table 1. Each section was evaluated by maximum value of the σ_{m+b}. The biggest stress values were detected close the blade surface (begin or end of the section l = max/min). The lengths of the sections are different for each section position. The comparison between all of the blade designs, from the safety factors view, is summarized in following Table 2.

Safety factor K [-]		A-A	B-B	C-C
Solid blade		5,1	-	5,7
Coarse honeycomb str. s = 9mm		1,17	1,36	2,11
Fine honeycomb str. s = 4,5mm		3,28	2,22	1,85
Differences [%]	Solid/coarse	77,1	-	62,9
	Solid/fine	35,7	-	67,5

Table 2. Safety factor comparison

Solid blade reached the best results from the safety factor view. In both sections, safety factor over five (K > 5) was obtained. The worst results were detected for blade with coarse honeycomb structure, where coarse internal structures work as stress concentrator and maximum stress intensity rapidly increased. This was mainly due to the area size between the honeycomb structures. It means bigger deflection for coarse honeycomb structures. But in all cases, it could be said that the safety factor condition K > 1 has been fulfilled. Table 2 shows the decrease of the safety factor also in percentage for different type of honeycomb structures. The percentages were calculated as the differences in safety for each type of the blade. The base value for the percentage calculation was set as the value for the solid blade. The same procedure was used to calculate the percentage decrease in values of natural frequencies (Table 4) and weight of blades (Table 3). The weights of the solid blades and blades with honeycomb structures were summarized in following Table 3:

Type of blade	Weight
Solid blade	578,2 g
Coarse honeycomb str.	422 g (27% material save)
Fine honeycomb str.	439 g (24% material save)

Table 3. The weight comparison between various honeycomb structures.

Modal analyses

Geometry of the pump impeller was reduced to separate blade for this modal analyses. Fixed support was set as boundary condition on blade hub (thread part). Fixed support faces were visualized in Figure 18 by blue color [Oza 2020].

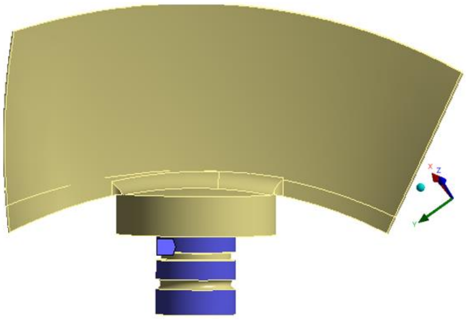

Figure 18. Geometry and boundary condition definition for modal analyses

For the modal analyses the same computational mesh was used as in FEM static simulations. These modal analyses were set up for surrounding air medium. We could expect that the modal analyses in water will have lower frequency values (approx. 60 – 80% from air values) [Cupr 2021]. All mentioned variants of the blades were evaluated with modal analyses. From the results, it can be seen that the first three natural frequencies have same direction of the deformation. The deformation of the blade will be in direction of oscillations. In Figure 20 direction of the oscillation was visualized. The first natural frequency (shape of the deformation) is visualized in Figure 19.

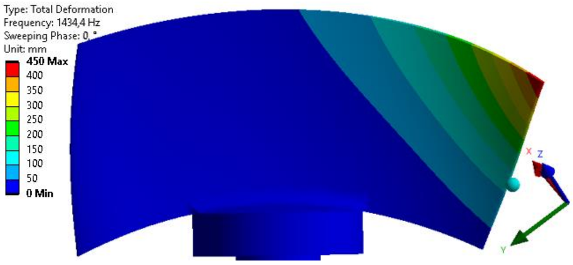

Figure 19. The first natural frequency of solid blade

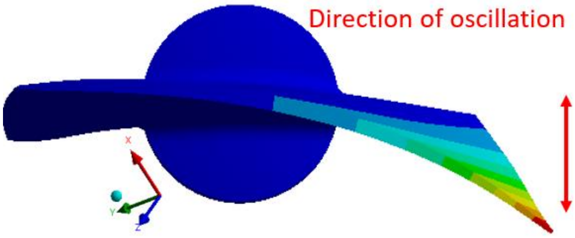

Figure 20. Direction of the first natural oscillation

In Figure 21, the first natural frequency of the blade with fine honeycomb structure is visualized. In this case it is evident, that value of natural frequency is lower. This is due to the loss of material on the blades, which reduces the overall stiffness of the blade.

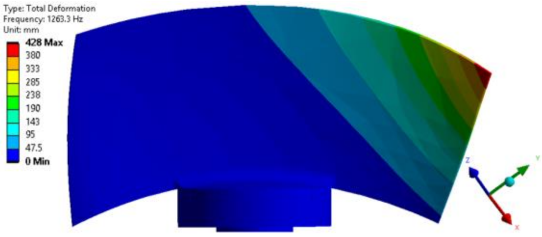

Figure 21. The first natural frequency of fine honeycomb structure blade

Table 4 shows first three natural frequencies, which are evaluated for all types of blades design.

Natural frequencies [Hz]		1.freq.	2.freq.	3.freq.
Solid blade		1 434	2 114	2 612
Coarse honeycomb str.		1 183	1 688	2 334
Fine honeycomb str.		1 263	1 798	2 239
Differences	Solid/coarse	17%	20%	10%
	Solid/fine	12%	15%	14%

Table 4. Overview of first three natural frequencies

Type of blade		Moment of inertia
Solid blade		0,217 kg·m^2
Coarse honeycomb str.		0,162 kg·m^2
Fine honeycomb str.		0,196 kg·m^2
Differences	Solid/coarse	25%
	Solid/fine	9%

Table 5. Moment of inertia comparison

4 3D METAL PRINTING

4.1 *Selective laser melting method (SLM)*

SLM is probably the most common method of 3D metal printing. The metals used are aluminium, steel, titanium, gold, silver, copper, nickel and cobalt-chromium alloys. The method consists of sintering and melting the metal powder applied in layers. First, a layer of powder is applied, followed by melting with a laser beam, the adjacent grains of the powder melt, sinter and blend. This is repeated in the layers until the product is finished. Figure 22 visualized the principal of the selective laser melting. The printing is performed in a protective atmosphere; the type of gas is chosen according to the powder metal used. Selective laser melting is a precise method, producing good-looking products with high surface quality compared to other 3D printing methods.

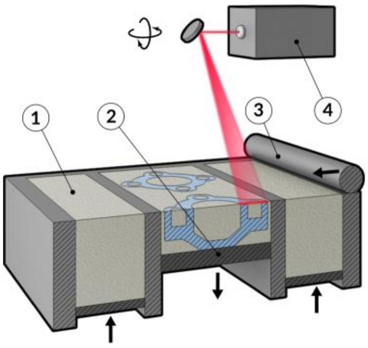

Figure 22. Principle of the selective laser melting (1 - powder metal container, 2 - displacement device, 3 - powder applicator, 4 - laser)

4.2 *Product shape inspection*

To verify the results of the shape accuracy of parts made by 3D printing, the finished parts can be scanned using an optical scanner and then compared with the original 3D CAD design. The scanning procedure is as follows. Auxiliary scanning points, which represent Figure 23 are glued to the scanned object on two sides, then both sides of the object are scanned using a turntable. After processing using appropriate software, a color map of deviations from the original CAD design is created, as shown in Figure 24.

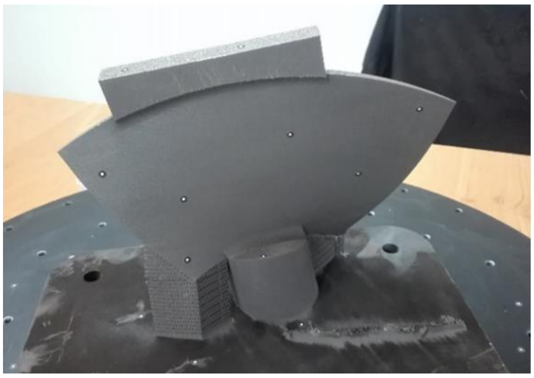

Figure 23. Object made by 3D printing with glued scanning points

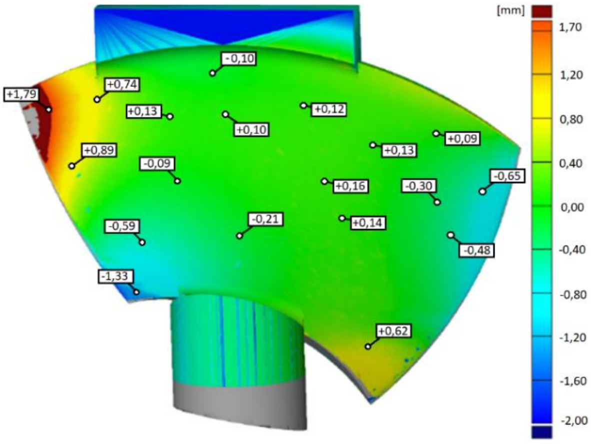

Figure 24. Color map of shape deviations

4.3 *3D blade printing*

Based on the experience of previous years with 3D printing of various parts of the samples, it was decided to use a laser power setting of 200 W for the printing of pump blades. The reason is to reduce the influence of thermal stresses that lead to the deformation of manufactured parts. This is especially true when printing large parts. Printing parameters were: Powder layer height 45 µm, fill track width 150 µm, laser power and speed are shown in following Table 6.

Support		**Contour**		**Fill**	
Power [W]	Speed [mm/s]	Power [W]	Speed [mm/s]	Power [W]	Speed [mm/s]
180	1200	200	1440	200	1200

Table 6. Print parameters

The pump blade has been made several times. Deformations were gradually eliminated in individual prints by changing the geometry of the supporting structures and the orientation of the part in the building space. Subsequently, a shape inspection was performed by comparing the original CAD model with a scan of the final product. Scanning was performed using an Atos Core 5M scanner. The scanned data are directly displayed in the GOM Scan software, and the subsequent comparison with the CAD data takes place in the GOM Inspect software. Shape inspection shows the accuracy of the product, as shown in Figure 24. Identified inaccuracies will be eliminated by modifying and strengthening the support structures.

4.4 *Printing of blades with internal honeycomb structure for hydrodynamic tests*

Based on the verification for the technology of production of blades with an internal honeycomb structure, the final blades for the hydrodynamic tests were made on the basis of a digital model, as shown in Figure 25. Figure 26 represents the blade on the construction board, where the construction supports can be seen, which prevent the shape of the blade from collapsing during the actual 3D printing. Excess powder inside honeycomb has been dumped through small holes inside honeycomb, as shown in Figure 25. After removing the supports, the blades were annealed to remove mechanical stresses at 550 °C with a temperature increase of 3 hours and then held at 550 °C for 6 hours. The cooling was spontaneous to room temperature. After annealing, the blades were surface mechanically treated with corundum powder sandblasting and ground with ceramic bodies. Figure 27 shows the blades after milling the auxiliary holders and threading.

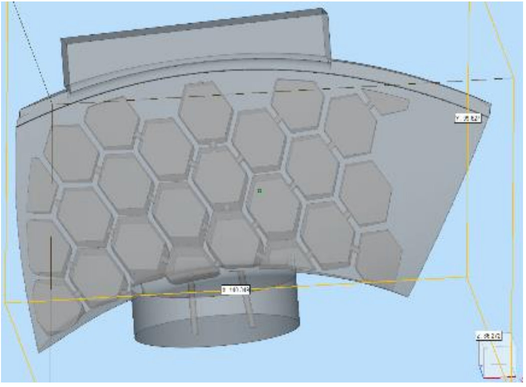

Figure 25. View of the inner honeycomb structure – model, holes for pouring powder are visible in bottom part

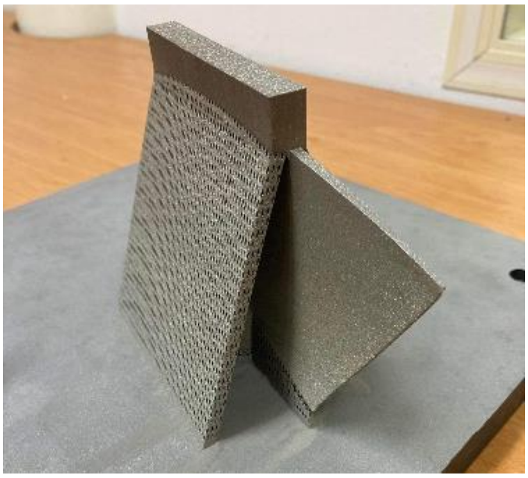

Figure 26. Blade on a construction board

Figure 27. Final blades

4.5 *Inspection of surface morphology and phase composition*

The properties of surfaces were studied by the methods of electron microscopy, digital optical microscopy, X-ray powder diffraction and Moessbauer spectroscopy, especially from the point of view of the order of postprocessing modifications of parts made by 3D printing by laser selective melting. The surfaces of three samples were compared: A - sample after 3D printing without modifications, B - sample sandblasted without annealing, C - sample sandblasted and annealed. Electron microscope images (Figure 28) show that the sandblasting removes residues on the surface of the welded spherical particles of the starting metal powder.

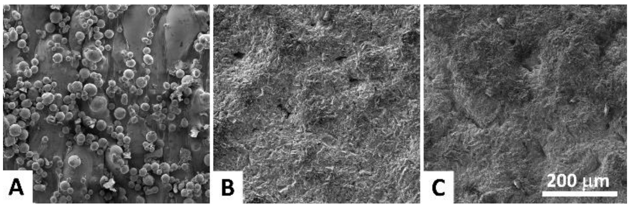

Figure 28. Electron microscope images (A - sample after 3D printing without modifications, B - sample sandblasted without annealing, C - sample sandblasted and annealed)

The evaluation of surface irregularities (roughness) was performed using digital optical microscopy, where the opportunity to evaluate the height of the surface irregularities was used. The results of inspecting the surface morphology with a digital optical microscope are shown in Figure 29. It is clear that the surface irregularities (roughness) of non-sandblasted samples are greater than the surface irregularities after sandblasting. Measurements showed that the maximum height of unevenness of non-sandblasted samples is greater than 130 µm (Figure 29 A), on the sandblasted sample the maximum height of unevenness is less than 50 µm. Of course, sandblasting has a dominant effect on surface roughness, but the pictures also show the effect of annealing.

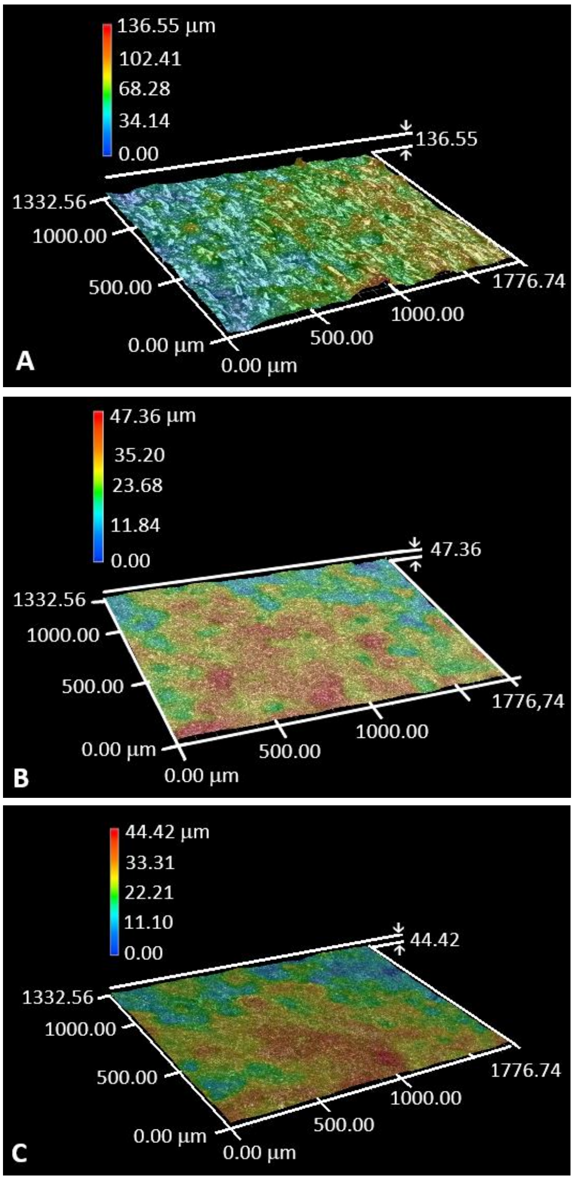

Figure 29 Surface morphology (A - sample after 3D printing without modifications, B - sample sandblasted without annealing, C - sample sandblasted and annealed)

The phase composition of the surface was studied by means of Moessbauer spectroscopy with conversion X-ray registration (CXMS) and conversion electron registration (CEMS) [Principi 2020]. Moessbauer spectroscopy with conversion electron registration (CEMS) provides us with information about the phase composition of the surface (depth given by the penetration of electrons through a material of about 1 µm). Moessbauer secondary X-ray spectroscopy (CXMS) provides information on the internal phase composition of the sample (depth given by the X-ray penetration of the material is approximately 200 µm). In Figure 30 (top - CXMS) it is clear that no phase changes occur due to sandblasting and following annealing in the sample volume. In all cases, only the austenitic phase of the stainless steel (singlet of the Moessbauer spectrum) was identified (FCC wall-centered grid). However, in the thin surface layer, approx. 0.5 µm, the CEMS method showed that the transformation of the austenitic phase to the ferritic phase occurs during the annealing of the sandblasted sample. This transformation occurs only in a thin surface layer, approx. 0.5 µm, (Figure 30 bottom – CEMS, sample C). In addition to the singlet corresponding to the austenitic phase, a sextet corresponding to iron in the alpha structural modification (BCC body-centered grid) is identified.

The phase composition was also studied by X-ray diffraction (XRD), which confirmed the results of Moessbauer spectroscopy. The XRD pattern of sample C, which was sandblasted and annealed after SLM manufacture, shows the presence of a BCC structure that corresponds to the ferritic phase (Figure 31). This result corresponds to the identification of the ferritic phase by CEMS (Figure 30 bottom, sample C).

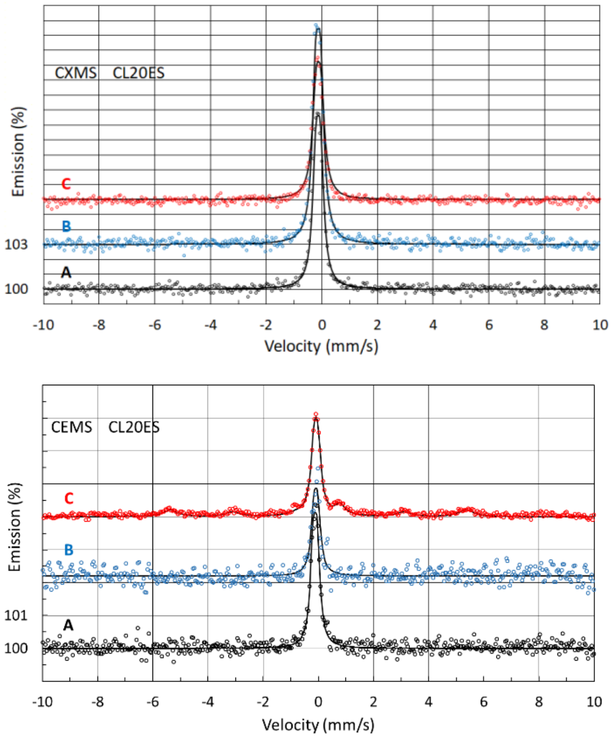

Figure 30. Moessbauer spectra CXMS - top, CEMS - bottom (A - sample after 3D printing without modifications, B - sample sandblasted without annealing, C - sample sandblasted and annealed)

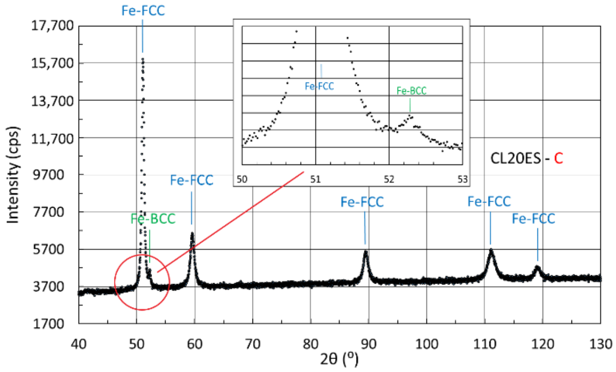

Figure 31. XRD pattern of sandblasted and annealed sample

5 CONCLUSIONS

The prediction of the hydraulic parameters of the pump with welded diffuser was fulfilled by the numerical simulations. The hydraulic efficiency at the design point reach over 90%. Maximum hydraulic efficiency was computed at part load operation (95% of the design point) and it reaches 91,9%. It is necessary to take into account decreasing hydraulic efficiency in real operation, caused by friction and mechanical loses. Influence of cavitation also may cause change in hydraulic parameters. The one-way FSI analyses were provided for optimal working conditions of the pump: Q = 330 $l \cdot s^{-1}$ and n = 1920 min^{-1}. Results are evaluated according to the standards [NTD A.S.I.]. It can be said that the use of the different types of honeycomb structures will lead to a rapid weight reduction, change of stress and strength properties and affects modal properties of the blades. In the static simulation were evaluated several parameters and it´s possible to defined following conclusion:

- First parameter was value of safety factor. All design met the condition K > 1. The best safety factor was evaluated for solid blade K = 5.
- The second parameter was weight of the blade. According to this parameter, the best result has the blade with coarse honeycomb structure. This blade has the highest value of material saving, around 27 % (blade weight: 422 g) of weight, with still good stiffness. This weight loss could slightly reduce moment of inertia which is visualized in Table 5.
- The third parameter was comparison of natural frequencies. This highest frequency has solid blade f = 1 434 Hz. Natural frequency decrease was connected with the material saving.

The blades with fine honeycomb structures were the best designs. Predictions of good results, in a term of honeycomb structures, were mentioned in literature, as ratio between weight and strength properties. A similar conclusion can be drawn from the analysed cases. This blade with inner structures accomplished all conditions that are set by [NTD A.S.I.]. It is necessary to say, that the internal structures work as internal stress concentrators, and for industrial use it must be analysed mechanical properties of the blades. 3D printing with metallic material can replace the complex production of prototype components and the creation of internal structures saves expensive basic powder material intended for 3D printing. The partial results, from our first experience with numerical simulations of honeycomb structures are presented in this article. It is clear, that there may be a number of more advantageous options of the inner structures. The best ratio of the blade weight and sufficient strength properties will be subject of the further research. The main focus will be on the finer inner structures, which can lead to better stress distribution inside the examined blade. This paper shows a possible way to simulate blades with internal structures – it must be noted that the research is still in its early stages and the results are not defnitive.

Digital optical microscopy has been shown to be used to study the morphological surface quality of parts made by 3D printing. However, scanning electron microscopy must be used to study the surface in more detail. The transformation of the austenitic phase into a ferritic phase activated by annealing at 550 °C was identified by Moessbauer spectroscopy and X-ray diffraction. The ratio of austenitic to ferritic phases in stainless steel is known to depend on the concentration of equivalent elements of chromium and nickel [Kraus 2015]. The connection between the identified transformation of the austenitic to ferritic phase in a thin surface layer and the concentration of chromium and nickel in stainless steel was shown in [Ivanova 2022]. Changes in phase composition and concentration of alloying elements in the surface layer may be important in relation to subsequent chemical surface treatments.

ACKNOWLEDGMENTS

This research was supported by Ministry of Education, Youth and Sports of the Czech Republic under the project CZ.02.1.01/0.0/0.0/17 049/0008408 "Hydrodynamic design of pumps".

Computational resources were supplied by the project "e-Infrastruktura CZ" (e-INFRA CZ LM2018140) supported by the Ministry of Education, Youth and Sports of the Czech Republic.

REFERENCES

[Gulich 2014] Gulich, J.F. Centrifugal pumps. Heidelberg: Springer, 2014. ISBN 978-3-642-40113-8.

[Karassik 2012] Karassik, I., Mcguire, J.T. Centrifugal pumps. Springer Science & Business Media, 2012. ISBN 978-1-4615-6606-9.

[Paciga 1984] Paciga, A., Stycek O., Ganco M. Cerpacia technika. Bratislava: Alfa, 1984.

[Pal 2020] Pal, A., Bertoldi K., Pham M., Schaenzer M., Gross A. Optimal turbine blade design enabled by auxetic honeycomb. Smart Materials and Structures [online]. 2020, 29(12) ISSN 0964-1726. Available from: doi:10.1088/1361-665X/abbd1d

[Novotny 2019] Novotny V., Spale J., Stunova B., Kolovratnik M., Vitvarova M., Zikmund P., 3D Printing in Turbomachinery: Overview of Technologies, Applications and Possibilities for Industry 4.0. In: Volume 6: Ceramics; Controls, Diagnostics, and Instrumentation; Education; Manufacturing Materials and Metallurgy [online]. American Society of Mechanical Engineers, 2019, 2019-06-17, s. ISBN 978-0-7918-5867-7. Available from: doi:10.1115/GT2019-91849

[Abhinav 2020] Abhinav, S.. (2020). A Review Paper on Origin of Honeycomb Structure and its Sailing Properties. International Journal of Engineering Research and. V9. 10.17577/IJERTV9IS080336.

[Wang 2019] Wang, Zhonggang. (2019). Recent advances in novel metallic honeycomb structure. Composites Part B: Engineering. 166. 10.1016/j.compositesb.2019.02.011.

[ANSYS 2022] ANSYS, Inc., 2016. ANSYS CFX User's Guide, Release 2019 R3.

[IEC 60 193] International Standard IEC 60 193: Hydraulic pumps, and pump-turbines – Model acceptance tests. International Electrical Commission. Genf. 1999.

[NTD A.S.I. Section 3] Sekce III, Hodnoceni pevnosti zarizeni a potrubi jadernych elektraren typu VVER. Asociace strojnich inzenyru, Praha, Brno 2020.

[NTD A.S.I. Section 2] Sekce II, Charakteristiky materialu pro zarizeni a potrubi jadernych elektraren typu VVER. Asociace strojnich inzenyru, Praha, Brno 2020

[Oza 2020] Oza, M.N., Shah, D.S., Theoretical and experimental modal analysis of centrifugal pump radial flow impeller. IOP Conference Series: Materials Science and Engineering [online]. 2020, 992(1). ISSN 1757-8981. doi:10.1088/1757-899X/992/1/012003.

[Cupr 2021] Cupr, P., Hydroelastic response of hydrofoil under cavitation conditions, Brno 2021.

[MAT.1.4301] CSN EN 10088-3: Stainless steels – part 3: Technical supply conditions for semi-finished products, bars, rolled wires, profiles and bright products made of corrosion-resistant steels for general use.

[Principi 2020] Principi, G. Metals, 2020, 10, 992. doi:10.3390/met10080992.

[Kraus 2015] Kraus, G. *STEELS* Processing, Structure, and Performance – second edition. ASM International, Materials Park, Ohio, 705pp, 2015.

[Ivanova 2015] Ivanova, T., Mashlan, M., Ingr, T., Dolakova, H., Sarychev, D., Sedlackova, A. Metals, 2020, 12, 551. doi.org/10.3390/met12040551.

CONTACTS:

Ing. Jakub Starecek, Ph.D.
CENTRE OF HYDRAULIC RESEARCH,
Jana Sigmunda 313, Lutin, 78349, Czech Republic
j.starecek@sigma.cz